Distinguishing Impacts on Winter Temperatures in Northern Mid–High-Latitude Continents during Multiyear and Single-Year La Niña Events: A Modeling Study

TINGTING ZHU[a] AND JIN-YI YU[a]

[a] *Department of Earth System Science, University of California, Irvine, Irvine, California*

(Manuscript received 18 May 2023, in final form 29 March 2024, accepted 8 April 2024)

ABSTRACT: Utilizing a 2200-yr CESM1 preindustrial simulation, this study examines the influence of property distinctions between single-year (SY) and multiyear (MY) La Niñas on their respective impacts on winter surface air temperatures across mid–high-latitude continents in the model, focusing on specific teleconnection mechanisms. Distinct impacts were identified in four continent sectors: North America, Europe, Western Siberia (W-Siberia), and Eastern Siberia (E-Siberia). The typical impacts of simulated SY La Niña events are featured with anomalous warming over Europe and W&E-Siberia and anomalous cooling over North America. Simulated MY La Niña events reduce the typical anomalous cooling over North America and the typical anomalous warming over W&E-Siberia but intensify the typical anomalous warming over Europe. The distinct impacts of simulated MY La Niñas are more prominent during their first winter than during the second winter, except over W-Siberia, where the distinct impact is more pronounced during the second winter. These overall distinct impacts in the CESM1 simulation can be attributed to the varying sensitivities of these continent sectors to the differences between MY and SY La Niñas in their intensity, location, and induced sea surface temperature anomalies in the Atlantic Ocean. These property differences were linked to the distinct climate impacts through the Pacific North America, North Atlantic Oscillation, Indian Ocean–induced wave train, and tropical North Atlantic–induced wave train mechanisms. The modeling results are then validated against observations from 1900 to 2022 to identify disparities in the CESM1 simulation.

KEYWORDS: Atmosphere–ocean interaction; Climate variability; ENSO

1. Introduction

El Niño–Southern Oscillation (ENSO) events typically span 1 year, commencing in the boreal spring, developing and intensifying during the subsequent summer and fall, and reaching their peak intensity in winter. Subsequently, they gradually weaken and transition into the opposite phase or turn to ENSO neutral phase in the following year. However, some ENSO events deviate from this pattern, persisting without transitioning into the opposite phase in the following year and becoming multiyear (MY) events. These are predominantly observed during the La Niña phase of ENSO rather than the El Niño phase (Hu et al. 2014; Okumura and Deser 2010). Understanding the underlying dynamics and distinct climatic impacts of MY La Niña events has attracted increasing interest and research efforts (e.g., Okumura et al. 2017; Iwakiri and Watanabe 2020; Zhu and Yu 2022; Nishihira and Sugimoto 2022; Kim et al. 2023).

Studies have suggested that MY La Niña events can cause severe droughts in the United States during the second winter of the events (Okumura et al. 2017), as well as warmer-than-normal summers in Japan (Iwakiri and Watanabe 2020). The Midwest in the United States suffers a warmer summer during the summer transitioning from an El Niño than during the summer persisting from a La Niña due to different teleconnections toward North America (Jong et al. 2020). MY La Niña events cause severe cold winters over East Asia during their first year and over northwestern North America during their second year (Nishihira and Sugimoto 2022). MY La Niña events were found to induce a three-season drought in the Horn of Africa (Anderson et al. 2023). The distinct climate impacts of MY La Niñas occur not only in the Northern Hemisphere but also in the Southern Hemisphere. Zhu and Yu (2022) found that the typical Antarctic sea ice anomaly pattern induced by single-year (SY) La Niña during the austral winter was displaced zonally during MY La Niña, attributable to an Indian Ocean memory mechanism. They found that the existence of a preceding-year strong El Niño condition, which overdischarges the equatorial Pacific Ocean heat continent and creates a favorable condition for MY La Niña events to occur, causes the Indian Ocean sea surface temperature (SST) conditions to be different between the MY and SY La Niña events. The diverse Indian Ocean SSTs induce distinct responses in the atmospheric circulation of the Southern Hemisphere to both the SY and MY La Niñas, leading to varied Antarctic sea ice anomaly patterns. In the present study, our objective is to investigate whether MY and SY La Niña events produce similar or different impacts on surface air temperatures (SATs) over mid–high-latitude continents in the Northern Hemisphere.

Previous studies suggest that ENSO events can significantly impact the climate of extratropical regions through diverse teleconnection mechanisms [e.g., the review by Yang et al. (2018)]. In the Northern Hemisphere, ENSO can initiate atmospheric wave trains propagating from the tropical Pacific to North America, giving rise to the Pacific North America (PNA) pattern (Wallace and Gutzler 1981). During La Niña events, this wave train can result in anomalous winter cooling in the northern United States and winter warming in the

---

Corresponding author: Jin-Yi Yu, jyyu@uci.edu

DOI: 10.1175/JCLI-D-23-0296.1

southern United States (Ropelewski and Halpert 1986; Yu et al. 2012). ENSO events can also influence extratropical climate by shifting atmospheric jet streams. During La Niña events, for example, the jet stream tends to shift poleward (Yuan 2004; Lu et al. 2008; Stachnik and Schumacher 2011), thereby inducing a positive phase of the North Atlantic Oscillation (NAO) (Brönnimann et al. 2007). This, in turn, triggers warmer-than-normal winters in Eurasia (Domeisen et al. 2019). Moreover, ENSO events can induce SST anomalies (SSTAs) in the adjacent tropical North Atlantic (TNA) and Indian Oceans through interbasin interaction processes [see reviewed by Cai et al. (2019)]. Typically, during La Niña events, there is an induced anomalous cooling of SST in the TNA region and the tropical Indian Ocean. The resultant TNA SSTAs can further initiate atmospheric wave trains that propagate downstream, impacting the climate in Eurasia (Lim 2015; Li and Ruan 2018). Similarly, the induced SSTAs in the Indian Ocean can trigger wave trains that influence the climate around the Pacific Rim (Annamalai et al. 2007; Min et al. 2008). However, it is unclear whether MY and SY La Niña events produce similar or different PNA, NAO, TNA SSTA-induced, and Indian Ocean SSTA-induced teleconnections, and how these four teleconnection mechanisms work together to shape the climate impacts of SY and MY La Niña events. This study addresses this issue.

The number of observed SY and MY La Niña events is restricted. This study employs a 2200-yr preindustrial simulation generated by NCAR's Community Earth System Model, version 1 (CESM1; Kay et al. 2015), to investigate the potential distinctive climate impacts of MY and SY La Niñas. The main goal is to evaluate how variations in La Niña properties between SY and MY events in a climate model can result in divergent climate impacts on mid–high-latitude continents. The model's findings may provide insights relevant to real-world occurrences. Recent studies have substantiated the CESM1 simulation's ability to replicate essential features of observed MY and SY ENSO events. These features include the spatial structures and temporal evolutions of their SST anomalies, as well as their teleconnections with adjacent Atlantic and Indian Oceans (Kim and Yu 2020, 2021, 2022; Zhu and Yu 2022; Kim et al. 2023; Lin and Yu 2023). Specifically, concerning La Niña events, Kim et al. (2023) have demonstrated that the CESM1 preindustrial simulation accurately captures the interactions between the tropical and extratropical Pacific associated with SY and MY La Niñas. Lin and Yu (2023) have shown that this CESM1 simulation reasonably reproduces not only the teleconnections of SY and MY La Niñas to the Atlantic and Indian Oceans but also the sensitivities of these teleconnections to ENSO properties. Additionally, Zhu and Yu (2022) have illustrated that this model simulation can generate reasonably realistic La Niña impacts and teleconnections to Antarctica.

In this study, we first utilize the substantial samples of MY and SY La Niña events in the CESM1 simulation to uncover the climate impacts on the mid–high-latitude continents and subsequently validate the model results using observed events. The data and methods employed are detailed in section 2, while the model results and observational verification are presented in sections 3 and 4. Section 5 concludes by summarizing the findings and discussing the implications of the study.

2. Data and methods

The NCAR preindustrial CESM1 simulation was run for 2200 years with greenhouse gas concentrations maintained at preindustrial levels. The fully coupled CESM1 model operated at ~1° horizontal resolution, with component models including the CAM5 atmospheric model, POP2 oceanic model, CLM4 land surface model, CICE4 sea ice model, and various other biogeochemical and chemical cycle models (Hurrell et al. 2013). For this study, data from model years 400 to 2200 of the simulation were utilized for analysis.

To assess the model's performance in simulating MY and SY La Niña events and their associated climate impacts, we conducted an analysis using observational and reanalysis data spanning from 1900 to 2022. The monthly SST data employed in this study are sourced from the Hadley Centre Sea Ice and Sea Surface Temperature dataset (HadISST; Rayner et al. 2003) with a horizontal resolution of 1°. Additionally, the monthly geopotential height, sea level pressure (SLP), and SAT data are obtained from the NCEP–DOE Reanalysis II dataset (Kanamitsu et al. 2002) with a horizontal resolution of 2.5° and the NOAA–CIRES–DOE Twentieth Century Reanalysis V3 dataset with a horizontal resolution of 1°. The Twentieth Century Reanalysis covers the period from 1900 to 1978, while the NCEP dataset spans from 1979 to 2022. We interpolate the Twentieth Century Reanalysis data to align with the resolution of the NCEP data and subsequently merge the two datasets for analyses. Monthly anomalies are calculated as the deviations from the monthly climatology after removal of the linear trend. The monthly climatologies for the model and observations are calculated as the means during their respective analysis periods.

Following Kim and Yu (2022), we use the 3-month running mean of the Ocean Niño index (ONI) to identify the MY and SY La Niñas in both the CESM1 simulation and observations. For example, the 3-month running mean of ONI for November is the average value over October–December. The ONI is defined as SSTAs averaged between 5°S–5°N and 170°–120°W. A La Niña event is identified when the running-mean ONI is less than -0.75 standard deviation (which is -0.85°C in the CESM1 simulation and -0.86°C in the observations) at any month from November^0 to January^{+1}. In this study, the year preceding the onset year of the La Niña event is denoted as year -1, while the onset year and the subsequent 2 years are denoted as years 0, $+1$, and $+2$, respectively. The months within these denoted years are labeled as month^{-1}, month^0, month^{+1}, and month^{+2}. A La Niña is identified as an MY (SY) event when its running-mean ONI falls below (above) 0°C during any month from November^{+1} to January^{+2}. Here, we used the threshold value 0°C instead of -0.5°C during the second year to attain more MY La Niña events. Applying this classification method, there are a total of 7 SY La Niña events and 15 MY events during the analysis period of 1900–2022 (Table 1).

We used four SST indices in the analysis. The Indian Ocean dipole (IOD) index (Saji et al. 1999) was defined as the

TABLE 1. Lists of MY and SY La Niña events during 1900–2022.

MY (15)	1908–10, 1916–18, 1933–35, 1942–44, 1949–51, 1954–56, 1970–72, 1973–75, 1983–85, 1988–90, 1995–97, 2007–09, 2010–12, 2020–22
SY (7)	1903/04, 1924/25, 1938/39, 1952/53, 1964/65, 2005/06, 2017/18

difference in SSTA between the western Indian Ocean (50°–70°E, 10°S–10°N) and the eastern Indian Ocean (90°–110°E, 10°S–0°). The zonal location (ZL) index of ENSO was defined as the difference between the SSTAs averaged over the tropical eastern Pacific (100°–160°W, 5°S–5°N) and those averaged over the tropical central Pacific (150°E–160°W, 5°S–5°N), following Kim and Yu (2022). A positive value of ZL indicates that the La Niña event is located more in the tropical central Pacific (CP) and is associated with the CP type of ENSO (Yu and Kao 2007; Kao and Yu 2009). Conversely, a negative ZL value indicates that the event is located more in the tropical eastern Pacific (EP) and is an EP type of ENSO. The ZL index is employed in all analyses exploring atmospheric and climatic reactions to various La Niña locations. The sole deviation is in Figs. 5e–h, where we utilized Niño-3 (5°N–5°S, 150°–90°W) and Niño-4 (5°N–5°S, 160°E–150°W) indices instead of the ZL index to illustrate the specific teleconnection responses to the EP and CP variants of La Niña. The cold tongue index (CTI) is defined as the SSTAs average between 180°–90°W and 6°S–6°N. Here, we use CTI instead of Niño-3.4 or ONI to measure the La Niña intensity because the CTI covers the central and eastern Pacific, providing a more precise measure of ENSO intensity, regardless of whether the ENSO event is of the EP or CP type. The TNA index is defined as the SSTAs averaged between 15°–55°W and 5°–25°N.

Two atmospheric teleconnections indices were also used in the study. Following CPC/NCEP (https://www.cpc.ncep.noaa.gov/products/precip/CWlink/pna/month_pna_index2.shtml), the PNA index is defined as a combination of 500-hPa geopotential height (Z500) anomalies at four centers:

$$\begin{aligned}\mathrm{PNA} = {} & \mathrm{Z500}(15^\circ - 25^\circ\mathrm{N}, 180^\circ - 140^\circ\mathrm{W}) \\ & - \mathrm{Z500}(15^\circ - 25^\circ\mathrm{N}, 180^\circ - 140^\circ\mathrm{W}) \\ & + \mathrm{Z500}(45^\circ - 60^\circ\mathrm{N}, 125^\circ - 105^\circ\mathrm{W}) \\ & - \mathrm{Z500}(25^\circ - 35^\circ\mathrm{N}, 90^\circ - 70^\circ\mathrm{W}).\end{aligned}$$

The NAO index is defined as the difference in area-averaged mean SLP between southern (90°W–60°E, 20°–55°N) and northern (90°W–60°E, 55°–90°N) boxes in the North Atlantic (Stephenson et al. 2006).

A two-tailed Student's t test was employed to evaluate the statistical significance of composite and regression analysis.

3. Single-year and multiyear La Niña properties and their climate impacts

a. *Differences in SSTA properties between SY and MY La Niñas*

The CESM1 preindustrial simulation produced a total of 351 La Niña events spanning years 400–2200, with 72% classified as MY events and 28% as SY events. These percentages closely align with observations during the analysis period of 1900–2022, where fifteen MY La Niña events (68%) and seven SY La Niña events (32%) were noted. Examining the composite evolution of the ONI (Fig. 1a), the simulated SY La Niña typically emerges in March^0–April^0–May^0 (MAM^0), peaks during December^0–January^1–February^1 (DJF^0), and then diminishes during MAM^{+1} before transitioning to an El Niño condition in June^{+1}–July^{+1}–August^{+1} (JJA^{+1}). Similar to the SY La Niña, the simulated MY La Niña initiates its development in MAM^0, reaching peak intensity during DJF^0. However, unlike the SY La Niña, the MY La Niña does not transition into an El Niño condition after its peak. Instead, the La Niña phase persists throughout the second year, diminishing in JJA^{+2} of the third year. The MY La Niña event reintensifies during the second year, displaying a secondary, weaker peak during DJF^{+1}, in contrast to the primary peak during DJF^0. The simulated ONI evolutions closely resemble those composited from the 7 SY and 15 MY La Niña events observed during the period 1900–2022 (Fig. 1d).

We then compared the composite SSTA patterns between the simulated MY and SY La Niñas, which revealed three key differences in the tropical Pacific and their associated SSTAs in the neighboring Atlantic and Indian Oceans. The first key difference is that MY La Niña is preceded by a strong El Niño event in the preceding year (Fig. 1c), whereas this is absent in SY La Niña (Fig. 1b). This aligns with observational studies suggesting that the occurrence of a preceding strong El Niño, resulting in an excessive discharge of the heat content in the tropical Pacific Ocean, is a pivotal factor in the formation of MY La Niña events (Dommenget et al. 2013; Hu et al. 2014; Larson and Pegion 2020; Iwakiri and Watanabe 2021). The second key difference lies in the location and intensity of the simulated La Niña SSTAs. While the simulated SY La Niña has its peak winter SST cooling in the tropical eastern Pacific, the cooling center of simulated MY La Niña shifts to the tropical central Pacific during both its first and second winters. This shift from the EP type to the CP type is also evident in the significant differences seen in the ZL index values between simulated SY and MY La Niñas (Fig. 2a). The ZL index shows a large negative value (indicating an EP type of La Niña) for the former, while the latter exhibits much smaller negative values during both its first (DJF^0) and second (DJF^{+1}) winters. The location shift is similar to what has been observed (see Fig. 2b). The variation in the La Niña location aligns with previous research findings, which suggested that the CP types of ENSO events are more proficient at activating the Pacific meridional mode (PMM) and its associated subtropical Pacific coupling processes, thereby extending the duration of ENSO events and leading to the emergence of MY events (Yu and Fang 2018; Fang and Yu 2020a,b; Kim and Yu 2022; Kim et al. 2023). Furthermore, the intensity of the simulated MY La Niña, as represented by the CTI, is stronger than that of SY La Niña during its first winter, but weaker during its second winter (Fig. 2a). Similar intensity changes can also be seen in the observations (see Fig. 2b), which has been noticed in Hu et al. (2014). The robust intensity of the MY La Niña in its first year makes it more challenging to

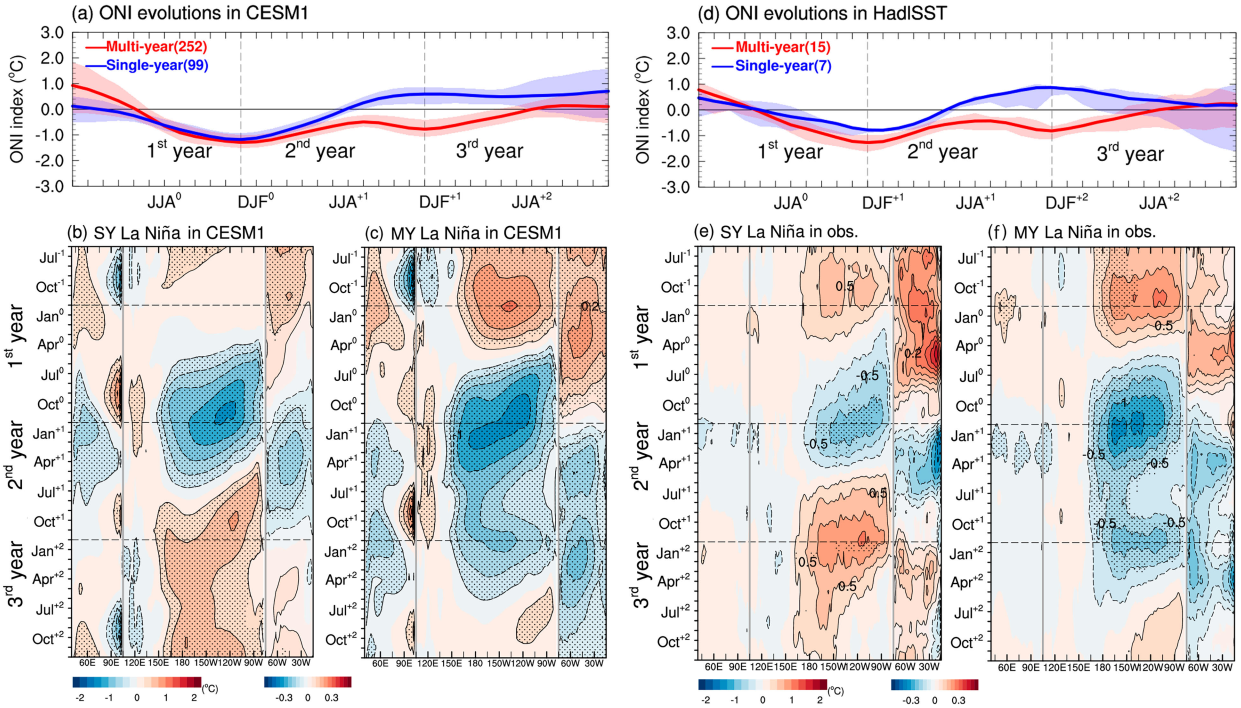

FIG. 1. Composite SSTAs of the SY and MY La Niñas simulated during years 400–2200 of the CESM1 preindustrial simulation: (a) ONI evolutions for the SY (blue line) and MY (red line) La Niña; (b) longitude–time plot of SSTAs along the equatorial (5°S–5°N) Indo-Pacific Oceans and tropical north (5°–25°N) Atlantic Ocean (shaded; °C) from June^{-1} to December^{+2} for the simulated SY La Niña; (c) as in (b), but for the simulated MY La Niña. (d)–(f) As in (a)–(c), with the difference being that they are composites based on the 7 SY La Niña events and 15 MY La Niña events observed during the period 1900–2022. Shadings in (a) and (d) indicate the interquartile ranges between the 25th and 75th percentiles. Dots in (b), (c), (e), and (f) indicate the areas where the shown values exceed the 95% confidence interval determined using a two-tailed Student's *t* test.

terminate, as it necessitates a greater recharge of the ocean heat content. Consequently, this condition should favor the persistence of La Niña into the following year (Hu et al. 2014).

The third key difference between the simulated MY and SY La Niñas appears in their accompanying SSTAs in the adjacent Atlantic and Indian Oceans. La Niña events are known to induce negative phases of the IOD and TNA through atmospheric bridge mechanisms, typically peaking during SON^0 and MAM^{+1}, respectively [see the review by Cai et al. (2019)]. These typical interbasin associations are also evident in the SSTA evolution composited during the simulated SY La Niña along the equatorial (5°S–5°N) Indo-Pacific Oceans and the subtropical (5°–25°N) North Atlantic (Fig. 1b). For the simulated MY La Niña (Fig. 1c), negative IOD and TNA features can be found during its first year (i.e., SON^0 and MAM^{+1}), but their magnitudes are weaker compared to those found in the SY La Niña. During the boreal winter, the values of the IOD and TNA indices are lower in the first year of the MY La Niña (i.e., DJF^0) compared to those of the SY La Niña (Fig. 2a). Zhu and Yu (2022) suggested that this third key difference is caused

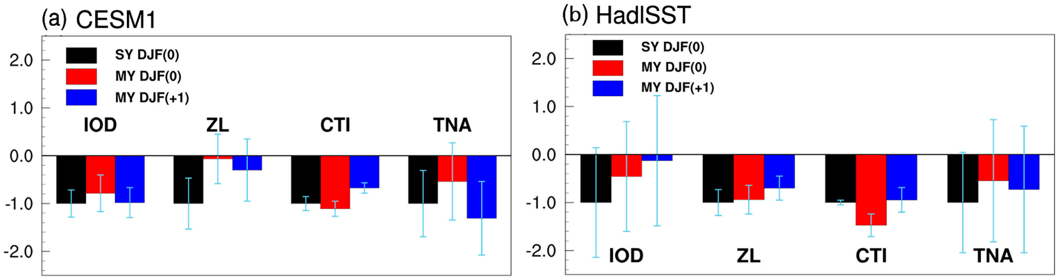

FIG. 2. (a),(b) Normalized values of the composite IOD, ZL, CTI, and TNA indexes for the SY La Niña during DJF^0 (black bars), and the DJF^0 (red bars) and DJF^{+1} (blue bars) of the MY La Niña. All values are normalized by the index value of the SY La Niña. The values shown in (a) are calculated from years 400 to 2200 of the CESM1 preindustrial simulation, and those in (b) are calculated from years 1900 to 2022 of the observations.

by the different preonset Pacific SSTA conditions between MY and SY La Niñas. The strong El Niño preceding the onset of MY La Niña triggers a basinwide warming in the Indian Ocean that lasted into the first developing year of MY La Niña (see Fig. 1c), counteracting the negative IOD typically induced by the La Niña. This explains why the simulated MY La Niña exhibits a weaker IOD during its first winter compared to that induced by the simulated SY La Niña. However, this residual effect from the preonset El Niño condition diminishes as the MY La Niña enters its second developing year, enabling the typical negative IOD condition to appear during the second winter (i.e., DJF^{+1}) of the event. The recovery of the IOD index, as illustrated in Fig. 2a, is evident when comparing the first and second winters of the simulated MY La Niña. The preonset El Niño condition also induces warm SSTAs over the tropical North Atlantic (between 5° and 25°N), persisting into the first developing year of the simulated MY La Niña and weakening the La Niña–induced TNA cooling during its first winter (see Fig. 1c). This explains the weakening of the TNA index value in the DJF^{0} of the simulated MY La Niña, with a ratio of 0.5 compared to the TNA index value in the simulated SY La Niña (Fig. 2a). In the second winter (DJF^{+1}), the negative TNA index value recovers and even strengthens with a ratio of 1.3. It is worth noting that the deviations of MY La Niña from SY La Niña in the CESM1 simulation are more pronounced for the TNA index than for the IOD index. Hence, the different SSTA conditions in the Atlantic Ocean may exert a greater influence than those in the Indian Ocean within the CESM1 simulation, serving as a source of distinct winter climate impacts between simulated MY and SY La Niñas.

We also investigated whether the three key differences we have identified are an artifact of the model biases or if they can be confirmed through observed SY and MY La Niña events. The observed SSTAs depicted in Figs. 1e and 1f affirm that the observed MY La Niñas are indeed preceded by a strong El Niño event, a pattern less evident in the case of the observed SY La Niñas. Nevertheless, the difference in this preonset condition between MY and SY La Niñas is less pronounced in the observations compared to the CESM1 simulation. This incongruity implies that the generation of simulated MY La Niñas is primarily influenced by the charge–discharge processes associated with the preceding strong El Niño, whereas the genesis of observed MY La Niñas involves other mechanisms. Recent studies have posited that subtropical Pacific processes, such as those linked to the seasonal footprinting mechanisms (Vimont et al. 2003), can also extend La Niñas to become MY events (Fang and Yu 2020a,b; Kim et al. 2023; Lin and Yu 2023). Evidently, these alternative processes play a more significant role in the emergence of observed MY La Niña events, whereas they are relatively less influential in the CESM1 simulation.

Turning to the second key distinction in the La Niña location and intensity, the observed La Niña also exhibits a more EP location for the SY La Niñas and a more CP location for the MY La Niñas (Figs. 1e,f). The values of their ZL index also underscore this divergence (Fig. 2b), although the index value difference between MY and SY La Niñas is smaller in the observations than in the CESM1 simulation. Hence, the location shift between MY and SY La Niñas is evident in both the CESM1 simulation and observations, with the shift being more pronounced in the former than the latter. The winter intensity of the observed MY La Niña is stronger than that of the observed SY La Niña during its first year but weaker than the SY La Niña during its second year, reaffirming what we found in the CESM1 simulation (see the CTI values shown in Fig. 2b).

The observed La Niña events also validate the third key difference regarding the impacts of La Niña on Atlantic and Indian Ocean SSTAs. The interbasin effects resulting from the strong El Niño preceding the onset of the observed MY La Niña persist into the initial development year of MY La Niña (Fig. 1f), counterbalancing the typical La Niña–induced cooling in the tropical North Atlantic and Indian Oceans. This residual impact is reflected by the reduced negative values of IOD and TNA indices in the first year of the observed MY La Niña compared to the SY La Niña (Fig. 2b). Similar to the CESM1 simulation, the TNA index rebounds in the second year of the observed MY La Niña once the residual impact diminishes. However, the IOD value during the second year of the observed MY La Niña remains quite low, challenging its identification as an IOD pattern in the observation. This stands in contrast to the findings in the CESM1 simulation. This contrast implies that IOD events in the CESM1 simulation are likely more influenced by ENSO events compared to what occurs in the observations.

In summary, the three key differences identified in the CESM1 preindustrial simulation between SY and MY La Niñas can largely be confirmed in the observations. However, these differences are more accentuated in the CESM1 than in the observations. While acknowledging that these disparities represent model biases and should be taken into account when interpreting results from the CESM1 preindustrial simulation, the accentuated distinctions also render the CESM1 simulation valuable for exploring the connections between the property differences of SY and MY La Niñas and the divergent climate impacts they generate.

b. *Differences in the impacts on winter temperature between MY and SY La Niñas*

We compare in Fig. 3 the composite winter SAT anomaly patterns between SY and MY La Niñas in the CESM1 simulation. The simulated SY La Niña leads to warmer-than-normal SATs over mid–high-latitude sectors in Eurasia, while colder-than-normal SATs appear across the same latitude zone in North America (Fig. 3a). The simulated MY La Niña exhibits a more complex SAT anomaly pattern in its first winter (Fig. 3b) compared to the SY La Niña. The SAT difference pattern between these two groups of La Niña (Fig. 3f) resembles the SAT anomaly pattern of the simulated SY La Niña but with opposite signs. This means that, in the CESM1 simulation, the MY La Niña overall reduces the SY La Niña–induced cooling over North America and warming over Eurasia. The only exception is over Europe where the SY La Niña–induced warming is intensified in the first winter of the simulated MY La Niña. Based on the magnitude of the difference, we divide

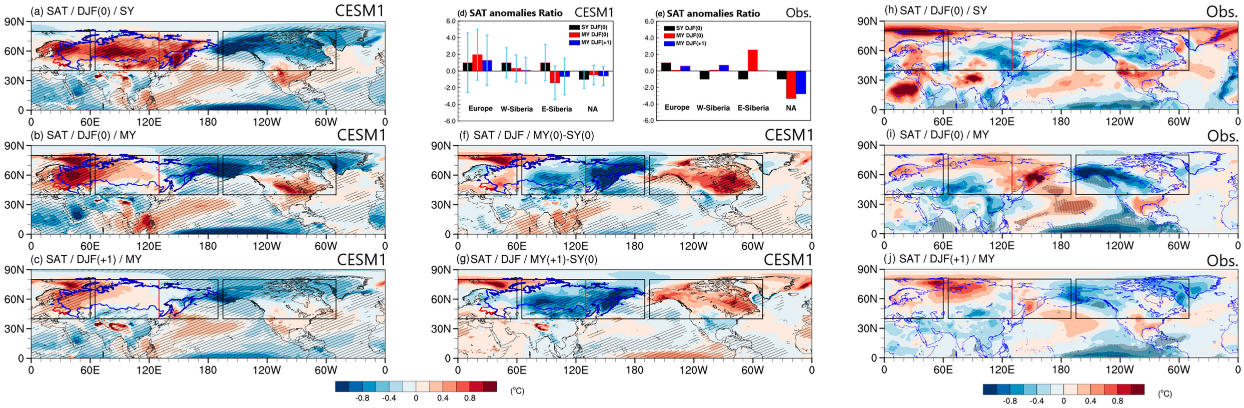

FIG. 3. SAT anomalies composited for (a) the boreal winter (DJF^0) of the simulated SY La Niña events, (b) MY La Niña's first boreal winter (DJF^0), and (c) MY La Niña's second boreal winter (DJF^{+1}) in the CESM1 preindustrial simulation; (d) the ratios of SAT anomalies averaged in the black box areas of Europe, W-Siberia, E-Siberia, and North America during the SY La Niña winter (black bars), MY La Niña's first winter (red bars), and MY La Niña's second winter (blue bars) compared to the SY La Niña value; (e) as in (d), but for the observed SY and MY La Niña events during the period 1900–2022; (f) the SAT difference between MY La Niña's first winter and SY La Niña winter; (g) the SAT difference between MY La Niña's second winter and SY La Niña winter; (h)–(j) as in (a)–(c), but for the observed SY and MY La Niña events during the period 1900–2022. The three black boxes from west to east in the figures are the areas of Europe, Siberia, and North America examined in the study. The red line in the second box further divides Siberia into W-Siberia and E-Siberia. Stippled regions in (a)–(c) and (h)–(j) indicate the areas where the values exceed the 95% confidence interval determined using a two-tailed Student's t test.

the mid–high-latitude continents into four sectors: North America, Europe, Western Siberia (W-Siberia; between 130°E and 170°W), and Eastern Siberia (E-Siberia; between 60° and 130°E). The positive SAT difference between MY and SY La Niñas over North America leads to a shift in winter temperature from colder-than-normal over southern Canada and the northern United States during SY La Niñas to warmer-than-normal during simulated MY La Niñas (cf. Figs. 3a and 3b). The negative SAT differences between MY and SY La Niñas over E&W-Siberia indicate that the regions of E&W-Siberia experience colder winters during simulated MY La Niñas compared to the warm winters encountered during simulated SY La Niñas. In fact, E-Siberia even encounters colder-than-normal winters during the simulated MY events. Only over Europe do the already warmer-than-normal winters experienced during simulated SY La Niñas become even warmer during simulated MY events.

In the second winter (DJF^{+1}) of the simulated MY La Niña, the SAT anomaly pattern (Fig. 3c) resembles the pattern seen during the first winter (cf. Fig. 3b). However, while the SAT differences between the second winter and the winter of the simulated SY La Niña (Fig. 3g) exhibit similarities to the differences identified in the first winter (cf. Fig. 3f), the magnitudes of the differences are mostly smaller in the second winter than in the first winter. Thus, the most pronounced distinct winter temperature impacts of the simulated MY La Niña on mid–high-latitude continents, compared to the simulated SY La Niña, occur primarily during its first winter rather than its second winter. The only exception is W-Siberia, where the reduced warming caused by the simulated MY La Niña compared to the simulated SY La Niña not only continues from the first to the second winters but also exhibits a larger magnitude.

To quantify the impacts of the simulated SY and MY La Niñas, we calculate the area-averaged SAT anomalies over the four sectors. These values allow us to assess the signs and strengths of the changing impacts. To determine the relative changes (i.e., ratios), we normalize the SAT index values by the index values of the simulated SY La Niña. The ratios of the index values (Fig. 3d) clearly demonstrate that the simulated SY La Niña leads to an anomalous SAT warming over Europe and E&W-Siberia while causing an anomalous SAT cooling over North America. Compared to the impacts of simulated SY La Niña, during the first winter of simulated MY La Niña, there is a remarkable 95.8% strengthening of anomalous warming over Europe, a 69.4% reduction in warming over W-Siberia, and a shift from anomalous warming to anomalous cooling over E-Siberia. The anomalous SAT cooling over North America is reduced by 52.1%. These changes in the impacts on SAT compared to the simulated SY La Niña were less pronounced during the second winter of the simulated La Niña. This decline is evident in the recovery of the index values, which gradually approached the index value of the simulated SY La Niña. The only exception occurs in W-Siberia, where the change strengthened in the second winter to such an extent that the warm SAT anomalies induced by simulated SY La Niña nearly vanished.

We further compared the La Niña impacts simulated by CESM1 with those observed. Figures 3h–j illustrate the winter SAT anomalies composited for SY and MY La Niña events observed from 1900 to 2022. Our comparisons suggest that the La Niña impacts on winter SAT produced by CESM1 align mostly with observations over both the North America and Europe sectors but show less consistency in the W-Siberia sector and the least consistency in the E-Siberia sector. In the North America sector, both CESM1 simulation and observations reveal

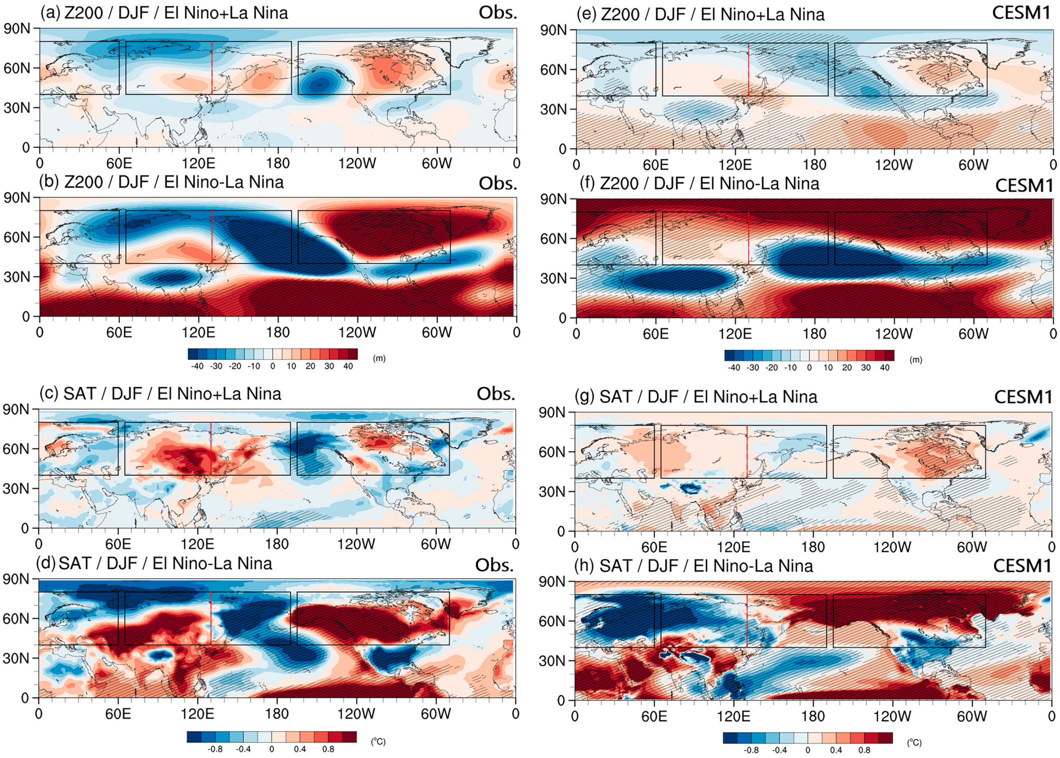

FIG. 4. (a),(c) The observed asymmetric and (b),(d) symmetric components of the ENSO responses for the composite anomalies of wintertime (DJF) 200-hPa geopotential height and SAT. The composites are calculated based on the El Niño and La Niña events observed during the period of 1900–2022. (e)–(h) As in (a)–(d), but calculated from the simulated El Niño and La Niña events in the years 400–2200 of the CESM1 preindustrial simulation. Stippled regions indicate the areas where the values exceed the 95% confidence interval determined using a two-tailed Student's *t* test.

predominantly negative SAT index values during SY and MY La Niñas (cf. Figs. 3d and 3e), with observations exhibiting stronger cooling. Over the Europe sector, CESM1 reproduces the observed anomalous SAT warming for both the La Niña types, but the simulated warming is generally stronger than observed (cf. Figs. 3a–c and 3h–j; Figs., 3d and 3e). In the W-Siberia sector, CESM1 reproduces observed anomalous SAT warming during the first and second winters of MY La Niña but fails to reproduce the observed anomalous cooling for SY La Niña (cf. Figs. 3d and 3e; Figs. 3a and 3h). The greatest inconsistency between CESM1 simulation and observations is found in the E-Siberia sector, especially for MY La Niñas (cf. Figs. 3d and 3e). Observations show overall anomalous cooling during SY La Niña winter and overall anomalous warming during both winters of MY La Niña (see Figs. 3e,h–j), whereas CESM1 produces opposite impacts in both SY and MY La Niña winters (see Figs. 3a–d). Overall, the impact differences between MY and SY La Niñas show consistency between observations and CESM1 simulations in North America and Europe but are less consistent in the E&W-Siberia sectors.

4. Differences in the impact mechanisms between MY and SY La Niñas

After identifying the distinct winter climate impacts of MY and SY La Niñas, we explored whether they can be linked to the three key differences in La Niña SSTAs between the MY and SY events through teleconnection mechanisms. For this part of the study, we primarily employed regression analyses to reveal the atmospheric responses and teleconnection patterns to various SSTA properties of La Niñas. It is widely acknowledged in studies (e.g., Hoerling and Kumar 1997) that the responses to La Niña and El Niño can be asymmetric. Consequently, regression analysis, which primarily reveals the symmetric component of ENSO responses, may not be suitable to explore the teleconnections to La Niña events if the asymmetric response is significantly large. Moreover, general circulation models may have difficulties in accurately replicating these asymmetries (e.g., Fang and Yu 2020b; Zhao and Sun 2022; references therein). To address this concern, we first examined the asymmetric and symmetric components of the winter [December–February (DJF)] 200-hPa geopotential height (Z200) and SAT responses to ENSO in both the observations and CESM1 simulation (Fig. 4). In the analysis, the symmetric component was calculated by subtracting the Z200/SAT anomalies composited for La Niña events from those composited for El Niño events, while the asymmetric component was determined as the sum of the El Niño and La Niña composites.

Our observational analysis reveals that the asymmetric component (Fig. 4a) in the Z200 response to El Niño and La Niña is considerably smaller than the symmetric component (Fig. 4b). Similar conclusions can be drawn regarding the asymmetric and symmetric components of the SAT response (cf. Figs. 4c and 4d). These findings align with Zhang et al. (2014), who suggested that the notable observed asymmetry in ENSO teleconnections between El Niño and La Niña phases may primarily be attributed to sampling variability. They used ensemble model experiments to demonstrate substantial variations in the magnitude of this asymmetric component across different ENSO events, leading to the conclusion that the authentic symmetric component likely exerts a more significant influence, underscoring the predominant role of symmetry in ENSO teleconnections. The CESM1 preindustrial simulation also produces a weaker asymmetric component in their Z200 (Fig. 4e) and SAT (Fig. 4g) responses to ENSO compared to the symmetric component (Figs. 4f,h). These results suggest that it is appropriate to use the regression analysis method to study the overall atmospheric responses to La Niña events in both the observations and the CESM1 simulation, even in the presence of nonnegligible asymmetric components in the responses.

Furthermore, we found that the CESM1 simulation replicates the overall Z200 and SAT patterns of observed symmetric and asymmetric responses more accurately over North America than over the Eurasian region of the mid–high-latitude continents. Consequently, the trustworthiness of the La Niña's climate impacts, as identified by this model, is more reliable in the North America sector than in the Eurasian sector. Furthermore, the model bias in Z200 simulations over the Eurasian region aligns with our finding that the discrepancies between the model and observations in the impacts on winter SATs are most pronounced in the W-Siberia and E-Siberia sectors, as discussed in section 3b (see Fig. 3).

a. Linking the PNA teleconnection mechanism to La Niña impacts on North America and W&E-Siberia

Regarding ENSO's teleconnection mechanisms, previous studies suggested that ENSO SSTAs can trigger the PNA wave train pattern, thereby influencing the climate in North America. This wave train can propagate downstream to impact the phase of the NAO and subsequently affect the climate in Eurasia. We first examine how these two teleconnection mechanisms operate during both the SY and MY La Niñas. Subsequently, we explore how the differences in SSTA characteristics between the MY and SY La Niñas affect these two mechanisms, thereby causing the overall differences in their winter impacts on North America and Eurasia.

In observations, La Niña typically excites a negative phase of the PNA pattern (Horel and Wallace 1981). This pattern (Fig. 5a) features two negative anomaly centers of Z200 over Hawaii and western Canada, as well as two positive Z200 anomaly centers over the southern Aleutian Islands and southeastern United States. The CESM1 simulation reproduces this observed negative PNA pattern very well (Fig. 5c). The CESM1 also reasonably simulates the variability of the observed PNA index, with the standard deviation of the PNA index in CESM1 ($\sigma = 79$) being similar to that in the observations ($\sigma = 96$). The SAT regressions onto the negative PNA index indicate that the negative PNA can induce anomalous cooling over North America and anomalous warming over W&E-Siberia in both the observations (Fig. 5b) and CESM1 simulation (Fig. 5d). In the CESM1 simulation, the PNA's impacts on North America and W&E-Siberia can be a result of thermal advection on the west and east sides of its positive Z200 anomaly center south of the Aleutian Islands (center B in Fig. 5c), supported by the 975-hPa wind anomalies regressed onto the PNA index (see Fig. 5d). By conducting an SAT regression onto the Z200 anomalies averaged over the area of center B (between 140°E–130°W and 35°–65°N) (Fig. 5j), we replicate the anomalous North America cooling and the anomalous E-Siberia warming seen in the PNA regression.

As discussed in section 3a, the locations of the MY La Niña during both the first and second winters are more concentrated over the central Pacific, while SY La Niña is situated over the eastern Pacific. To examine the impact of the location change on the PNA teleconnection mechanism, we conducted a multiple regression analysis of Z200 anomalies onto four key SST indices, namely, the Niño-3, Niño-4, IOD, and TNA indices. A similar multiple regression was also applied to SAT anomalies to reveal the individual impact of each of these four SST indices to SAT variations. The utilization of multiple regressions allowed us to isolate the specific effects of each of these four SST indices, minimizing the influence from other indices. Utilizing the multiple regressions, we find that in the CESM1 simulation, the multiple regression coefficient pattern of Z200 anomalies on Niño-3 (Fig. 5e) bears a closer resemblance to the PNA pattern (see Fig. 5c) than the corresponding multiple regression coefficient pattern on Niño-4 (Fig. 5g). While the Niño-3 regression coefficient pattern shows a positive center of Z200 anomalies south of the Aleutian Islands, the Niño-4 regression coefficient pattern exhibits a negative anomaly center. The multiple regression coefficient pattern of SAT anomaly onto the Niño-3 index in the CESM1 simulation (Fig. 5f) revealed anomalous cooling over North America and anomalous warming over W&E-Siberia. Consistent with the opposing Z200 anomalies, the multiple regression coefficient pattern of the SAT anomaly pattern onto the Niño-4 index is also out of phase with that onto the Niño-3 index (cf. Figs. 5h and 5f). Our results align with Okumura et al.'s (2017) assertion that the atmospheric teleconnection associated with observed La Niña events is sensitive to the geographical location of La Niña.

In the CESM1 simulation, as the SY La Niña is situated more in the tropical eastern Pacific, we find that its composite winter Z200 anomaly pattern (Fig. 5i) resembles the Z200 multiple regressions onto the Niño-3 index (see Fig. 5e), exhibiting a positive anomaly center south of the Aleutian Islands. Its composite winter SAT anomaly pattern (see Fig. 3a) similarly resembles the Niño-3-regressed SAT anomaly patterns over North America and W&E Siberia sectors (see Fig. 5f). This similarity implies that the PNA teleconnection mechanism is pivotal in generating the SY La Niña's impacts on winter SAT over the North America and W&E-Siberia sectors in the CESM1 simulation. Since the simulated MY La Niña is situated more in the tropical central Pacific (i.e., the Niño-4 region) during both the first and second winters, the composite Z200 anomalies for these two winters (Figs. 5k,l) mirror the Z200 anomaly pattern regressed onto Niño-4 (refer to Fig. 5g).

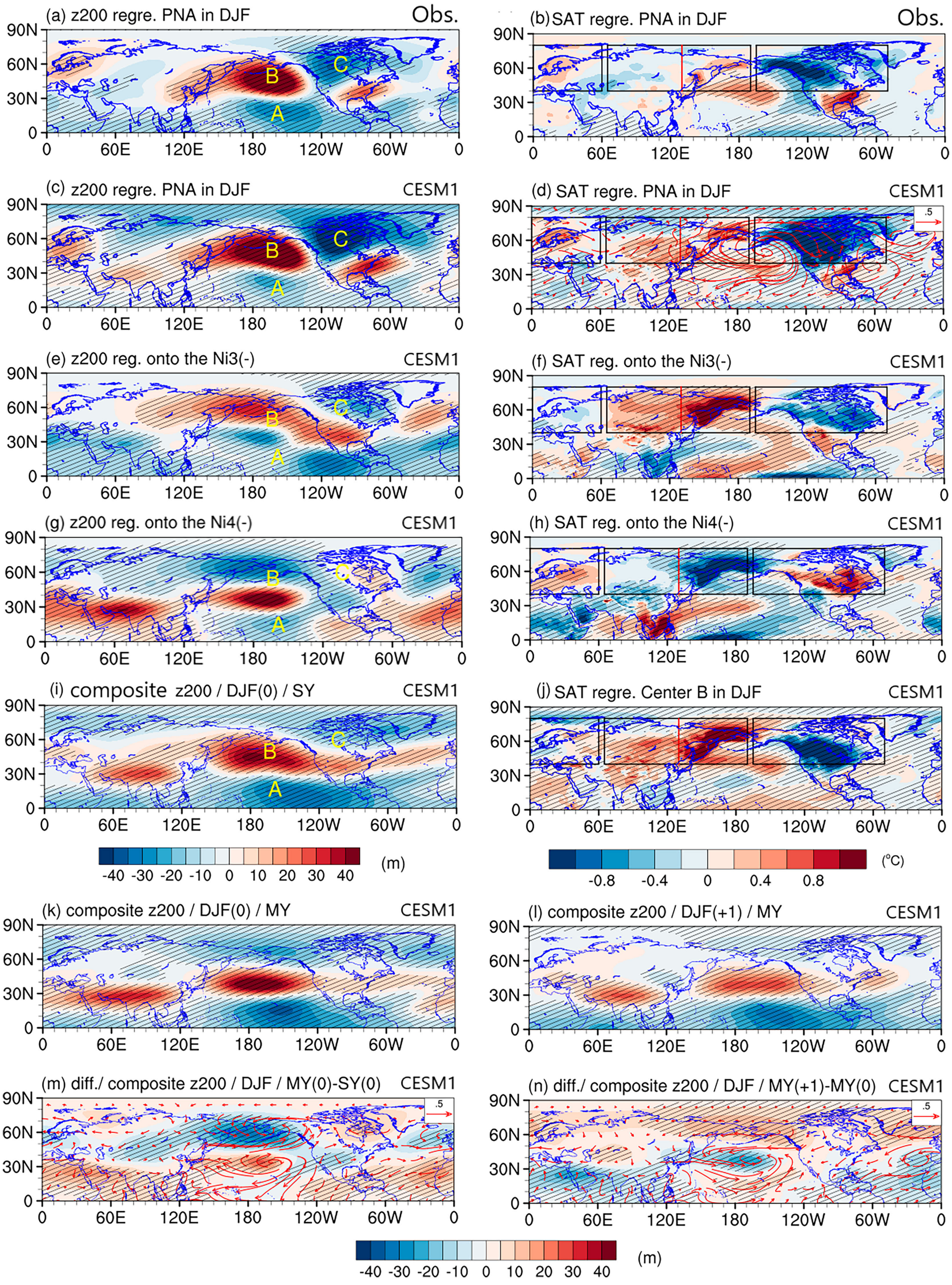

FIG. 5. Multiple regressions of (a) observed Z200 anomalies and (b) SAT onto the negative PNA index in boreal winter (DJF) during the period 1900–2022; multiple regressions of the simulated (c) Z200, (d) SAT (shaded), and 975-hPa wind (red vector) onto the negative PNA index during the boreal winter (DJF); multiple regressions of the simulated (e) Z200 anomalies and (f) SAT anomalies onto the negative Niño-3 index; (g),(h) as in (e) and (f), but for regression onto the negative Niño-4 index; (i) composite Z200 anomalies during the boreal winter (DJF^0) of the simulated SY La Niñas; (j) regression of the simulated SAT anomalies onto the averaged Z200 over center B during the boreal winter (DJF); composite Z200 anomalies during (k) the first boreal winter (DJF^0) and (l) the second boreal winter (DJF^{+1}) of the simulated MY La Niñas; (m) the composite Z200 difference between the simulated SY and the MY La Niñas during the first boreal winter (DJF^0); (n) the composite Z200 difference and 975-hPa wind difference (red vector) between the second winter (DJF^{+1}) and the first winter (DJF^0) of the simulated MY La Niña. Centers A–C mark the PNA anomaly centers in (c). Stippled regions indicate the areas where the values exceed the 95% confidence interval determined using a two-tailed Student's *t* test.

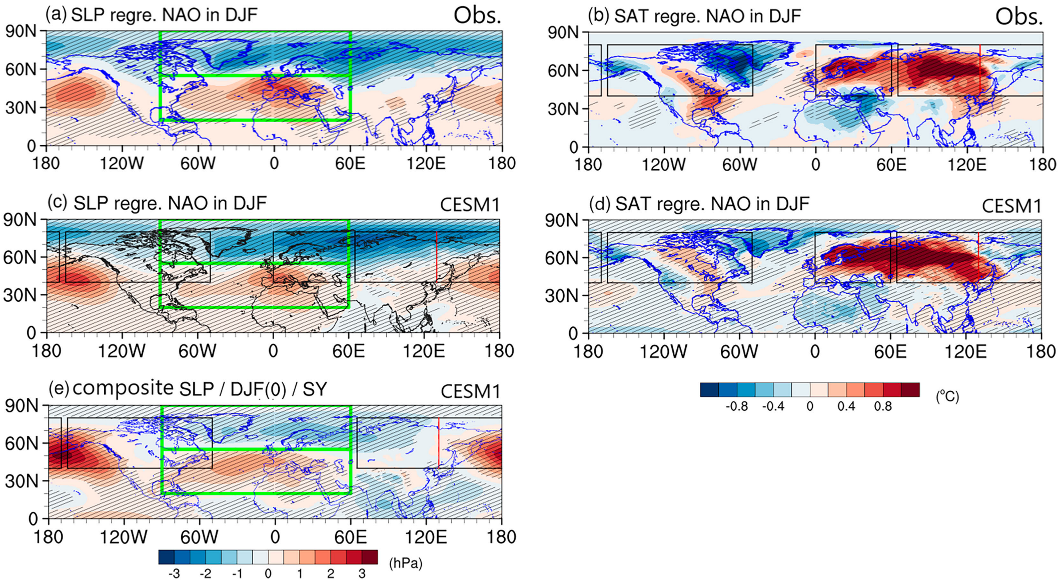

FIG. 6. Regressions of (a) observed SLP anomalies and (b) observed SAT onto the positive NAO index in boreal winter (DJF) during the period 1900–2022; regression of (c) SLP and (d) SAT anomalies onto the positive NAO index during the boreal winter (DJF) in the CESM1 preindustrial simulation; (e) composite SLP anomalies during the boreal winter (DJF^0) of the simulated SY La Niñas. Green thick boxes in (a), (c), and (e) mark the region of the NAO pattern. Stippled regions indicate the areas where the values exceed the 95% confidence interval determined using a two-tailed Student's *t* test.

Their composite winter SAT anomaly patterns (see Figs. 3b,c) also resemble the Niño-4-regressed SAT anomaly patterns over North America and W&E Siberia sectors (see Fig. 5h). The largest Z200 anomaly difference between the first winter of the simulated MY and SY La Niñas occurs over the Aleutian Islands (Fig. 5m). This negative Z200 difference leads to warm advection to North America, reducing the anomalous cooling induced by the simulated SY La Niña through the PNA teleconnection mechanism, and cold advection over W&E-Siberia, reducing the anomalous warming induced by the simulated SY La Niña. Thus, the overall reduction of the simulated SY La Niña's impacts on SAT over North America and W&E-Siberia sectors during the first winter of the simulated MY La Niña is attributed to the westward shift in the La Niña location.

As the intensity of the simulated MY La Niña diminishes from its initial to subsequent winters, the Pacific wave train triggered by SSTAs in the Niño-4 region is weaker in the second winter in comparison with the first (Fig. 5n). This explains why the reduction effect of the simulated MY La Niña on the impacts of SY La Niña on winter SATs diminished from its first to the second winter over the North America and W&E-Siberia sectors. It is interesting to note that Nishihira and Sugimoto (2022) found that the observed MY La Niña induced more significant anomalous cooling over northwestern North America during its second winter compared to the first winter. The heightened anomalous cooling they emphasized aligns with the diminished anomalous warming revealed by the CESM1 simulation. While they attributed this variation to diverse adiabatic heating in the tropical northwestern Pacific during the two winters of observed MY La Niña events and the resulting fluctuations in wave train propagation, our modeling study suggests that disparate La Niña intensities between the two winters can be another factor contributing to distinct impacts on North America.

b. *Linking the NAO teleconnection mechanism to La Niña impacts on Europe and W-Siberia*

Next, we investigated the role of the NAO teleconnection mechanism in shaping the La Niña impacts on winter SATs over Eurasia, as well as changes in this mechanism between SY and MY events. Previous studies have demonstrated that La Niñas can trigger a positive phase of the NAO by converging wave activity fluxes associated with the downstream extending of the PNA it generates from the Pacific (Pinto et al. 2011). The CESM1 simulation produces a realistic NAO pattern (Fig. 6c), with an anomalous surface low near Iceland and an anomalous surface high near the Azores Islands, consistent with the observed pattern (Fig. 6a). The positive NAO is associated with the northward shift of the polar jet stream (Hall et al. 2015). This shift confines cold air toward the pole, resulting in anomalous SAT warming in mid–high-latitude regions. The warming pattern is clearly depicted in the SAT regression onto the observed NAO index (Fig. 6b). The CESM1 simulation reproduces this NAO impact, as evidenced by the SAT regression onto the simulated NAO index (Fig. 6d). In the CESM1 simulation, the negative NAO induces a warming effect that is particularly pronounced over Europe and the W-Siberia sectors. We find that the composite winter SLP anomalies of the simulated SY La Niña (Fig. 6e)

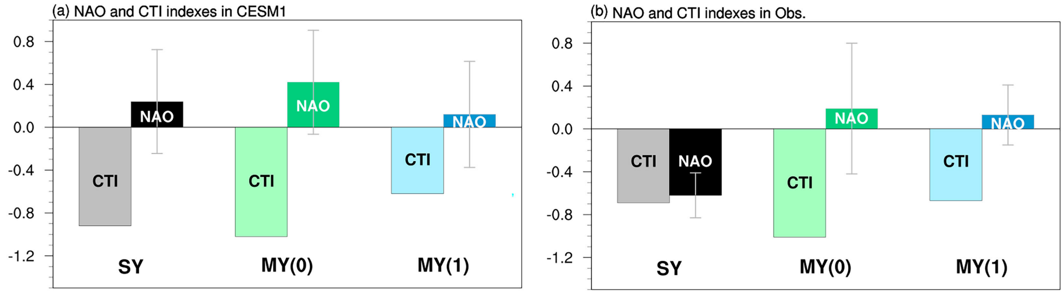

FIG. 7. The values of the composite NAO (dark bars) and CTI (light bars) indices during the SY La Niña winter (black), MY La Niña's first (green), and MY La Niña's second winter (blue) in the (a) CESM1 and (b) observation during the period 1900–2022. The error bars overlaying on NAO bars are one standard deviation of NAO values.

closely resemble the positive NAO pattern over the North Atlantic. Therefore, the NAO teleconnection mechanism is one of the factors contributing to the anomalous winter warming induced by the simulated SY La Niña over Europe and W-Siberia (see Fig. 3a).

We further explore how changes in the La Niña intensity and location influence the effectiveness of the NAO teleconnection mechanism in shaping the impacts on SAT as La Niñas change from SY to MY events. In the CESM1 simulation, the NAO index exhibits a significant negative correlation with the CTI ($R = -0.22$; p value = 0.0). This correlation implies that as the intensity of La Niña strengthens, it becomes increasingly likely to trigger a more pronounced positive NAO pattern. This relationship is consistent with the modeling finding reported by Hardiman et al. (2019). However, there is no significant correlation between the NAO index and the ZL index ($R = -0.013$; p value = 0.57), indicating that the NAO is not sensitive to changes in the zonal location of La Niña. In line with the La Niña intensity control, the composite NAO index value is the greatest during the first winter of the simulated MY La Niña (CTI = −1.02°), followed by the second greatest value during the simulated SY La Niña winter (CTI = −0.92°), and the smallest value during the second winter of the simulated MY La Niña (CTI = −0.62°) (Fig. 7a). The greater peak intensity during the first winter of MY La Niña, compared to SY La Niña, enables the former to produce a stronger NAO response. This explains why the first winter of the simulated MY La Niña induces more pronounced warming over Europe compared to the simulated SY La Niña (see Fig. 3f). Similarly, since the La Niña intensity during the second winter of simulated MY La Niña is weaker than that of simulated SY La Niña, the weaker NAO it induces elucidates why the warming over Europe during the second winter is milder compared to the warming caused by simulated SY La Niña (see Fig. 3g). We find a similar relationship between NAO intensity and MY La Niña intensity in the observation (Fig. 7b). The composite NAO value in the first winter (NAO = 0.19, CTI = −1.01) is greater than that in the second winter (NAO = 0.13, CTI = −0.67) of the observed MY La Niña. However, the relationship between NAO and CTI for the observed SY La Niña (NAO = −0.69, CTI = −0.62) is different from what was found for the simulated SY La Niña. It remains undisclosed whether this discrepancy is a result of model deficiency or is caused by the limited number of SY La Niña events in the observations.

Given that the NAO influence is more pronounced during the first winter of the simulated MY La Niña compared to the simulated SY La Niña winter, one would anticipate a stronger anomalous SAT warming over W-Siberia in the MY La Niña. However, contrary to this expectation, as shown in Fig. 3d, the warming over Siberia is actually less pronounced in the simulated MY La Niña compared to the simulated SY La Niña. The discrepancy arises from the fact that simulated La Niña events can influence winter SATs over W-Siberia through both the NAO and PNA teleconnection mechanisms. Evidently, the anomalous warming driven by the NAO mechanism is partially counteracted by the anomalous cooling induced by the PNA mechanism during the first winter of the simulated MY La Niña. As elucidated in a previous section, the westward positioning of MY La Niña in the CESM1 simulation facilitates the PNA teleconnection mechanism to shift the wave pattern across the North Pacific, introducing an anomalous cooling effect on winter SATs over Siberia. The cancelation effect of the PNA mechanism on the NAO mechanism is not found during the simulated SY La Niña, as both mechanisms contribute to anomalous warming over W-Siberia for this group of La Niñas. In the second winter of the simulated MY La Niña, the weaker NAO influence coupled with the attenuated PNA influence collectively leads to the observed small SAT anomalies, as depicted in Fig. 3d.

c. *Linking the TNA-excited wave train mechanism to La Niña impacts on Europe*

A third impact mechanism of ENSO is related to ENSO's ability to induce SSTAs in the TNA region. The induced TNA anomalies can further trigger atmospheric wave trains that propagate downstream and affect the climate in Eurasia. Previous research demonstrated that a La Niña event can lead to cold SSTAs in the TNA region. Both the observation (Fig. 8a) and CESM1 simulation (Fig. 8b) reveal that the multiple regression coefficient pattern of Z200 anomalies onto the TNA index is characterized by a wave train that propagates from the TNA to Eurasia. The wave train exhibits positive anomaly centers over the TNA (referred to as "D" in Fig. 8b) and Europe (referred to as "F"), along with a negative anomaly center over eastern Canada (marked as "E").

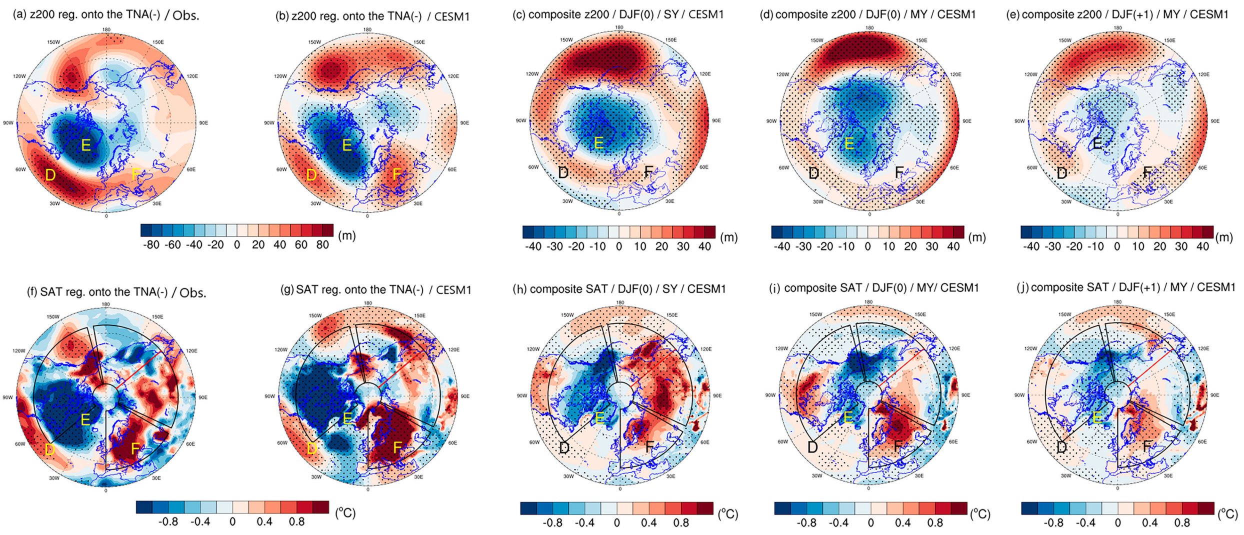

FIG. 8. Multiple regressions of (a) observed Z200 anomalies and (f) observed SAT anomalies onto the negative TNA index in boreal winter (DJF) during the period 1900–2022; multiple regressions of boreal winter (DJF) (b) Z200 and (g) SAT anomalies onto the negative TNA index in the CESM1 preindustrial simulation; composite Z200 anomalies during (c) the boreal winter (DJF^0) of the simulated SY La Niñas; (d) the first boreal winter (DJF^0) and (e) the second boreal winter (DJF^{+1}) of the simulated MY La Niñas, which are the same as Figs. 5i, 5k, 5l but with a different map projection for the sake of comparison; composite SAT anomalies during (h) the boreal winter (DJF^0) of the simulated SY La Niñas, (i) the first boreal winter (DJF^0), and (j) the second boreal winter (DJF^{+1}) of the simulated MY La Niñas, which are the same as Figs. 3a–c, but with a different map projection for the sake of comparison. Stippled regions indicate the areas where the values exceed the 95% confidence interval determined using a two-tailed Student's *t* test. Centers D–F mark the Z200 anomaly centers of the wave train excited by TNA [based on (b)].

Corresponding to the negative Z200 anomaly in center F, an anomalous warm SAT center was observed over the European sector. This is evident in the multiple regression coefficient pattern of SAT anomaly onto the TNA index conducted with both the observations (Fig. 8f) and the CESM1 simulation (Fig. 8g). The three anomaly centers of the TNA-induced wave train are discernible in the composite Z200 anomalies of the simulated SY La Niña (Fig. 8c). Hence, the TNA-induced wave train mechanism is a contributing factor to the anomalous winter warming produced in the Europe sector during the simulated SY La Niña (Fig. 8h, reproduced from Fig. 3a for comparison purposes).

In the simulated MY La Niña, the three anomaly centers of the TNA-induced wave train are also evident in its Z200 anomaly composites during both the first and second winters (Figs. 8d,e). As previously mentioned, the simulated MY La Niña exhibits a weaker negative TNA index than the simulated SY La Niña during its first winter but a stronger negative TNA index during its second winter (cf. Figs. 1b and 1c). The composite TNA value progressively amplifies from nearly 0 during the first winter to about −0.2 during the second winter (Fig. 9). However, the overall amplitude of the composite Z200 anomalies is larger during the first winter rather than during the second winter. This is because the NAO teleconnection mechanism is strong during the first winter of the MY La Niña, driven by the strong CTI intensity associated with the MY La Niña during this period. Consequently, the TNA-induced wave train is less influential than the NAO mechanism in affecting SAT variations over the Europe sector during the first winter of the simulated MY La Niña. The TNA influence gains prominence during the second year of the simulated MY La Niña when the La Niña–induced TNA anomalies reach a value even larger than that found during the simulated SY La Niña. This is evidenced by the heightened prominence of Z200 anomalies in center F of the TNA-induced wave train during the second winter compared to the first winter. This strong TNA influence explains why the SAT warming over the Europe sector remains stronger during the second winter of the simulated MY La Niña compared to the winter of the simulated SY La Niña, despite the NAO teleconnection mechanism being weakened due to the weaker CTI intensity in the former than the latter.

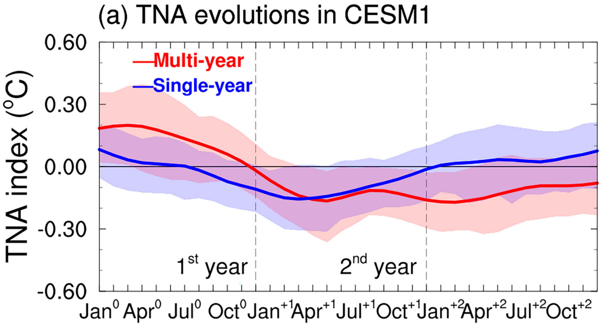

FIG. 9. Evolution of the TNA index during the simulated SY and MY Niñas in the CESM1 preindustrial simulations. Shadings indicate the interquartile ranges between the 25th and 75th percentiles.

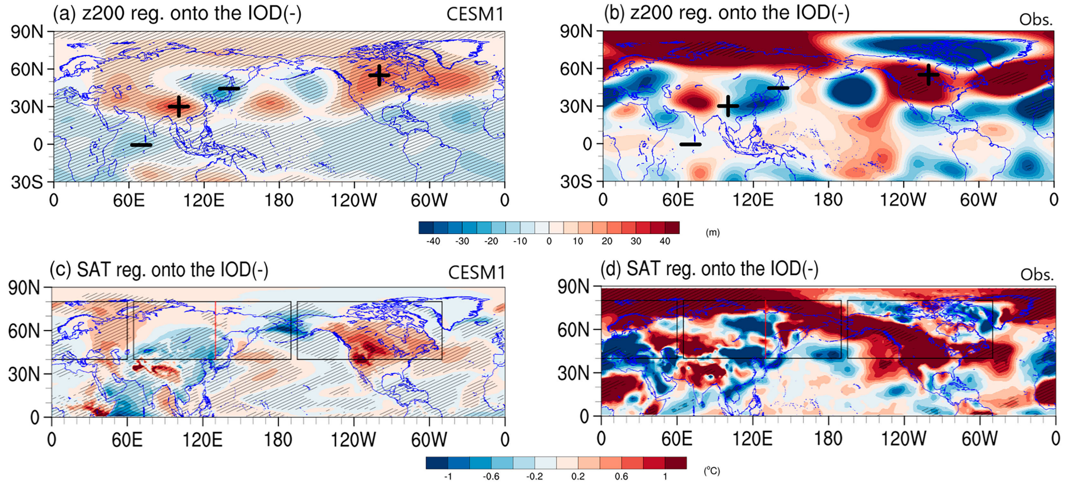

FIG. 10. Multiple regressions of (a) Z200 and (c) SAT anomalies regressed onto the negative IOD index during the boreal winter (DJF) of the CESM1 preindustrial simulation. (b),(d) As in (a) and (c), respectively, but with calculations based on observational data spanning the analysis period from 1900 to 2022. Three black boxes from west to east are the areas of Europe, Siberia, and North America. Stippled regions indicate the areas where the values exceed the 95% confidence interval determined using a two-tailed Student's *t* test. The "+" and "−" signs indicate the center of positive and negative anomaly centers associated with the IOD-induced Pacific-Rim wave train, respectively.

d. Linking the Indian Ocean–excited wave train mechanism to La Niña impacts on North America

Last, the negative IOD initiated by La Niña can also instigate a wave train propagating along the western Pacific Rim (Annamalai et al. 2007; Min et al. 2008), influencing the climatic impacts associated with La Niña. Multiple regression analysis of Z200 and SAT anomalies onto the simulated and observed IOD index reveals that the negative phase of the IOD can stimulate an atmospheric wave propagating across the Pacific Rim to North America (Figs. 10a,b). This can result in anomalous winter warming over North America in both the CESM1 simulation (Fig. 10c) and observations (Fig. 10d). Therefore, both the IOD and PNA patterns can affect Z200 and SAT anomalies over North America. Despite this, when examining composite winter SAT anomalies over the North American sector during both simulated SY and MY La Niñas (see Fig. 3), it is apparent that the warming effect produced by the IOD teleconnection mechanism is overshadowed by the cooling effect from the PNA teleconnection mechanism. Based on the regression coefficient values derived from the SAT regressions with the IOD and PNA indices (cf. Figs. 5d and 10c), it is evident that one standard deviation of the IOD index causes a 0.14 standard deviation of SAT warming over the North America sector, while one standard deviation of the PNA index induces a more substantial −0.79 standard deviation of SAT cooling. Consequently, the IOD-induced warming over North America does not manifest in the winter SAT anomaly composites during both the simulated SY and MY La Niñas (see Figs. 3a–c).

It should be noted that previous studies have found the IOD to be important in causing climate variations over East Asia (Zhang et al. 2022a,b; Chen et al. 2018). In our study, we also find that the IOD contributes to SAT anomalies in both Southern and Northern China in the CESM1 simulation (see Fig. 10c). The simulated IOD also induces SAT anomalies over Europe and W-Siberia, but the magnitudes of these anomalies are relatively small compared to the SAT anomalies induced by the NAO in these two regions (see Fig. 6d). In E-Siberia, it is noteworthy that the IOD-induced SAT anomalies in the CESM1 simulation are very minimal. Based on these findings, we conclude that in the CESM1 simulation, the teleconnection mechanism associated with the La Niña–induced IOD does not provide a significant explanation for the influence of La Niña on winter temperatures in the mid-to-high latitudes.

5. Summary and discussion

The main goal of this study is to utilize the long-term CESM simulation to gain insights into how SSTA differences between SY and MY La Niñas can lead to remote variations in SAT across the North America–Europe–Siberia sector in the model through specific teleconnection mechanisms. Acknowledging discrepancies between the model and observations, it is necessary to emphasize that this modeling study can still contribute to understanding the distinct climate impacts produced by SY and MY La Niñas. Additionally, the model discrepancies identified in this study provide insights into assessing the performance of the long-term CESM1 simulation, which has been increasingly utilized in the studies of the dynamics and climate impacts of MY ENSOs.

Based primarily on the CESM1 preindustrial simulation, our results indicate that during the first winter, the simulated MY La Niña generally weakened the typical warming impacts over Eurasia and cooling impacts over North America, which are commonly associated with the simulated SY La Niña. The

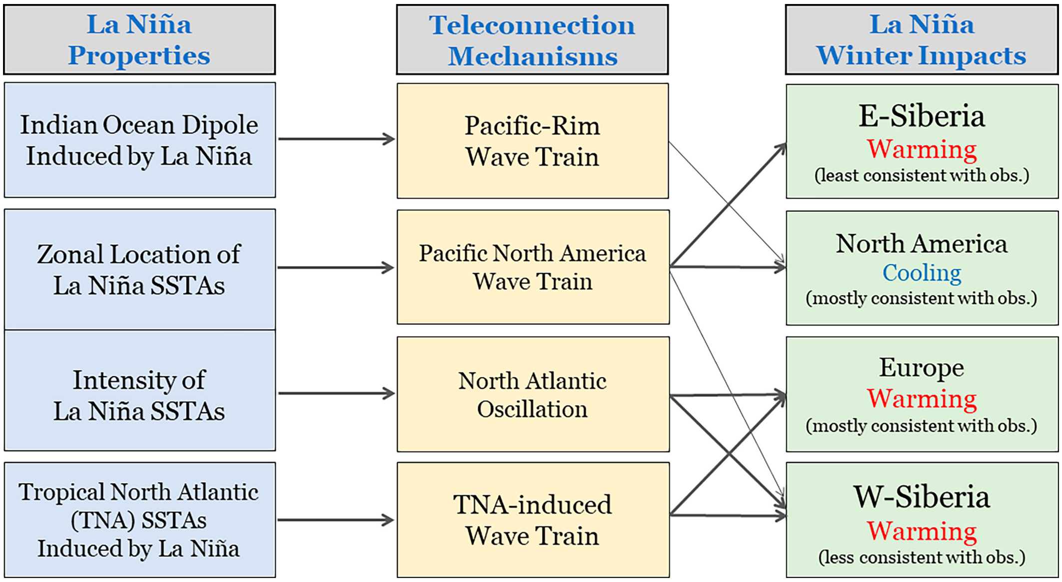

FIG. 11. A schematic illustrating, based primarily on the CESM1 preindustrial simulation, how (left) La Niña properties affect its impacts on winter temperatures over four key regions of the (right) mid–high-latitude continents through (middle) various teleconnection mechanisms. The La Niña properties include the ZL and intensity inside the Pacific, negative IOD inside the Indian Ocean, and negative TNA inside the Atlantic Ocean. The four key regions are North America, Europe, W-Siberia, and E-Siberia. The teleconnection mechanisms are the Pacific-Rim wave train, negative PNA (PNA−), positive NAO (NAO+), and TNA-induced wave train. Think solid arrows indicate the strong effects, and thin solid arrows indicate the weak effects. The labels "Warming" and "Cooling" in the "La Niña Winter Impacts" column are derived from the effects found during the CESM1-simulated SY La Niñas and may vary from those found during simulated MY La Niñas. The information displayed below these labels in the same column indicates whether the simulated impacts are consistent or not consistent with the impacts found during the observed SY La Niña events spanning from 1900 to 2022.

differences in impacts decreased from the first to the second winters of the simulated MY events, indicating that the distinctive influence of MY La Niña on winter temperatures is most pronounced during its first winter but becomes less distinct compared to SY events during the second winter. There are two notable deviations from the general impact of MY La Niña described above. The first exception manifests in Europe, where the warming influence of the simulated SY La Niña was heightened during the first winter of MY La Niña. The second exception arises in W-Siberia, where the distinct winter temperature effects generated by the simulated MY La Niña are even more pronounced in the second winter.

This study also concluded that, in the CESM1 simulation, the impacts of La Niña on winter SATs over North America and Eurasia are primarily determined by the intensity and location of the La Niña-related SSTAs and the associated Atlantic SSTAs it induces. The La Niña–induced SSTAs in the Indian Ocean were found to be less significant in this regard. Our modeling findings are summarized in the illustration shown in Fig. 11. Specifically, the SSTA location of La Niña has the greatest influence on the extent of anomalous cooling over North America and anomalous warming over W&E-Siberia in the CESM1 simulation due to its control over the propagation path of the PNA teleconnection mechanism. The intensity of La Niña plays a crucial role in determining the extent of anomalous warming over Europe and W-Siberia, as it affects the effectiveness of the NAO teleconnection mechanism. Last, the La Niña–induced SSTAs in the TNA region have a significant impact on winter temperature responses over Europe through the TNA-induced wave train mechanism.

Based on our analyses, Fig. 11 leads to the conclusion that La Niña–induced impacts on SAT are primarily determined by the PNA and IOD teleconnections over the North America sector in the CESM1 preindustrial simulation, with the former being much more influential than the latter. In the Europe sector, these impacts are shaped by the NAO and TNA teleconnections. In the W-Siberia sector, they are influenced by both the NAO and PNA teleconnections. In the E-Siberia sector, the impacts on SAT are solely determined by the PNA teleconnection. The solid lines connecting the mechanism boxes in the second column of Fig. 11 with impacts on SAT in the third column indicate the specific teleconnection mechanisms that are either primary or secondary in determining the La Niña impacts on SAT in each specific sector of the mid–high-latitude continent. The differences in winter SAT anomalies between the first winter of the MY La Niña and SY La Niñas were diminished in the second year of the MY La Niña over North America, Europe, and E-Siberia. This reduction is attributed to the return of the zonal location and intensity of the MY La Niña aligning with those of the SY La Niña.

The impacts on SAT presented in the third column of Fig. 11 also provide a summary indicating that the impacts on SAT resulting from SY and MY La Niñas in the CESM1 preindustrial simulation are in best agreement with the observations over both the North America and Europe sectors, less consistent with the observations over W-Siberia, and least consistent with the observations over E-Siberia.

The findings of this study present an opportunity to utilize the properties of La Niña-related SSTAs within and beyond the tropical Pacific to comprehend and forecast the changing impacts associated with MY La Niña events compared to the typical impacts of SY events. For example, if a La Niña event is projected to be a MY event, we should expect atypical winter climate impacts to occur primarily during its first winter, rather than the second winter. By considering the La Niña location and intensity, as well as the SSTAs induced in the tropical North Atlantic, it may be possible to predict the potential changes in winter impacts across various regions of mid–high-latitude continents. Nonetheless, it should be noted that the cause-and-effect relationships inferred in this study need to be further verified with numerical experiments. The findings reported here are model dependent since they rely solely on the CESM1 model.

Acknowledgments. We would like to express our gratitude to Editor Mingfang Ting and anonymous reviewers for their constructive comments, which have greatly contributed to the improvement of this paper. This research is supported by NSF Climate and Large-Scale Dynamics Program under Grant AGS-2109539. The authors are grateful to all data providers.

Data availability statement. The 2200-yr CESM1 preindustrial control simulation can be accessed from Earth System Grid (https://www.cesm.ucar.edu/projects/community-projects/LENS/data-sets.html). The observed SIC data come from the Met Office Hadley Centre (https://www.metoffice.gov.uk/hadobs/hadisst/data/download.html). The Reanalysis II data are available from the website (https://psl.noaa.gov/data/gridded/data.ncep.reanalysis2.html). The NOAA–CIRES–DOE Twentieth Century Reanalysis V3 can be accessed from the website (https://www.psl.noaa.gov/data/gridded/data.20thC_ReanV3.html).

REFERENCES

Anderson, W., B. I. Cook, K. Slinski, K. Schwarzwald, A. McNally, and C. Funk, 2023: Multiyear La Niña events and multiseason drought in the horn of Africa. *J. Hydrometeor.*, **24**, 119–131, https://doi.org/10.1175/JHM-D-22-0043.1.

Annamalai, H., H. Okajima, and M. Watanabe, 2007: Possible impact of the Indian Ocean SST on the Northern Hemisphere circulation during El Niño. *J. Climate*, **20**, 3164–3189, https://doi.org/10.1175/JCLI4156.1.

Brönnimann, S., E. Xoplaki, C. Casty, A. Pauling, and J. Luterbacher, 2007: ENSO influence on Europe during the last centuries. *Climate Dyn.*, **28**, 181–197, https://doi.org/10.1007/s00382-006-0175-z.

Cai, W., and Coauthors, 2019: Pantropical climate interactions. *Science*, **363**, eaav4236, https://doi.org/10.1126/science.aav4236.

Chen, J., X. Wang, W. Zhou, C. Wang, Q. Xie, G. Li, and S. Chen, 2018: Unusual rainfall in Southern China in decaying August during extreme El Niño 2015/16: Role of the western Indian Ocean and north tropical Atlantic SST. *J. Climate*, **31**, 7019–7034, https://doi.org/10.1175/JCLI-D-17-0827.1.

Domeisen, D. I. V., C. I. Garfinkel, and A. H. Butler, 2019: The teleconnection of El Niño Southern Oscillation to the stratosphere. *Rev. Geophys.*, **57**, 5–47, https://doi.org/10.1029/2018RG000596.

Dommenget, D., T. Bayr, and C. Frauen, 2013: Analysis of the non-linearity in the pattern and time evolution of El Niño southern oscillation. *Climate Dyn.*, **40**, 2825–2847, https://doi.org/10.1007/s00382-012-1475-0.

Fang, S.-W., and J.-Y. Yu, 2020a: Contrasting transition complexity between El Niño and La Niña: Observations and CMIP5/6 models. *Geophys. Res. Lett.*, **47**, e2020GL088926, https://doi.org/10.1029/2020GL088926.

——, and ——, 2020b: A control of ENSO transition complexity by tropical Pacific mean SSTs through tropical-subtropical interaction. *Geophys. Res. Lett.*, **47**, e2020GL087933, https://doi.org/10.1029/2020GL087933.

Hall, R., R. Erdélyi, E. Hanna, J. M. Jones, and A. A. Scaife, 2015: Drivers of North Atlantic polar front jet stream variability. *Int. J. Climatol.*, **35**, 1697–1720, https://doi.org/10.1002/joc.4121.

Hardiman, S. C., N. J. Dunstone, A. A. Scaife, D. M. Smith, S. Ineson, J. Lim, and D. Fereday, 2019: The impact of strong El Niño and La Niña events on the North Atlantic. *Geophys. Res. Lett.*, **46**, 2874–2883, https://doi.org/10.1029/2018GL081776.

Hoerling, M. P., and A. Kumar, 1997: Why do North American climate anomalies differ from one El Niño event to another? *Geophys. Res. Lett.*, **24**, 1059–1062, https://doi.org/10.1029/97GL00918.

Horel, J. D., and J. M. Wallace, 1981: Planetary-scale atmospheric phenomena associated with the Southern Oscillation. *Mon. Wea. Rev.*, **109**, 813–829, https://doi.org/10.1175/1520-0493(1981)109<0813:PSAPAW>2.0.CO;2.

Hu, Z.-Z., A. Kumar, Y. Xue, and B. Jha, 2014: Why were some La Niñas followed by another La Niña? *Climate Dyn.*, **42**, 1029–1042, https://doi.org/10.1007/s00382-013-1917-3.

Hurrell, J. W., and Coauthors, 2013: The community Earth system model: A framework for collaborative research. *Bull. Amer. Meteor. Soc.*, **94**, 1339–1360, https://doi.org/10.1175/BAMS-D-12-00121.1.

Iwakiri, T., and M. Watanabe, 2020: Multiyear La Niña impact on summer temperature over Japan. *J. Meteor. Soc. Japan*, **98**, 1245–1260, https://doi.org/10.2151/jmsj.2020-064.

——, and ——, 2021: Mechanisms linking multi-year La Niña with preceding strong El Niño. *Sci. Rep.*, **11**, 17465, https://doi.org/10.1038/s41598-021-96056-6.

Jong, B.-T., M. Ting, R. Seager, and W. B. Anderson, 2020: ENSO teleconnections and impacts on U.S. summertime temperature during a multiyear La Niña life cycle. *J. Climate*, **33**, 6009–6024, https://doi.org/10.1175/JCLI-D-19-0701.1.

Kanamitsu, M., W. Ebisuzaki, J. Woollen, S.-K. Yang, J. J. Hnilo, M. Fiorino, and G. L. Potter, 2002: NCEP–DOE AMIP-II reanalysis (R-2). *Bull. Amer. Meteor. Soc.*, **83**, 1631–1644, https://doi.org/10.1175/BAMS-83-11-1631.

Kao, H.-Y., and J.-Y. Yu, 2009: Contrasting eastern-Pacific and central-Pacific types of ENSO. *J. Climate*, **22**, 615–632, https://doi.org/10.1175/2008JCLI2309.1.

Kay, J. E., and Coauthors, 2015: The Community Earth System Model (CESM) large ensemble project: A community resource for studying climate change in the presence of internal climate variability. *Bull. Amer. Meteor. Soc.*, **96**, 1333–1349, https://doi.org/10.1175/BAMS-D-13-00255.1.

Kim, J.-W., and J.-Y. Yu, 2020: Understanding reintensified multi-year El Niño events. *Geophys. Res. Lett.*, **47**, e2020GL087644, https://doi.org/10.1029/2020GL087644.

——, and ——, 2021: Evolution of subtropical Pacific-onset El Niño: How its onset location controls its decay evolution. *Geophys. Res. Lett.*, **48**, e2020GL091345, https://doi.org/10.1029/2020GL091345.

——, and ——, 2022: Single- and multi-year ENSO events controlled by pantropical climate interactions. *npj Climate Atmos. Sci.*, **5**, 88, https://doi.org/10.1038/s41612-022-00305-y.

——, ——, and B. Tian, 2023: Overemphasized role of preceding strong El Niño in generating multi-year La Niña events. *Nat. Commun.*, **14**, 6790, https://doi.org/10.1038/s41467-023-42373-5.

Larson, S. M., and K. Pegion, 2020: Do asymmetries in ENSO predictability arise from different recharged states? *Climate Dyn.*, **54**, 1507–1522, https://doi.org/10.1007/s00382-019-05069-5.

Li, J., and C. Ruan, 2018: The North Atlantic–Eurasian teleconnection in summer and its effects on Eurasian climates. *Environ. Res. Lett.*, **13**, 024007, https://doi.org/10.1088/1748-9326/aa9d33.

Lim, Y.-K., 2015: The East Atlantic/West Russia (EA/WR) teleconnection in the North Atlantic: Climate impact and relation to Rossby wave propagation. *Climate Dyn.*, **44**, 3211–3222, https://doi.org/10.1007/s00382-014-2381-4.

Lin, Y.-F., and J.-Y. Yu, 2023: The role of Indian Ocean in controlling the formation of multi-year El Niños through subtropical ENSO dynamics. *J. Climate*, **37**, 385–401, https://doi.org/10.1175/JCLI-D-23-0297.1.

Lu, J., G. Chen, and D. M. W. Frierson, 2008: Response of the zonal mean atmospheric circulation to El Niño versus global warming. *J. Climate*, **21**, 5835–5851, https://doi.org/10.1175/2008JCLI2200.1.

Min, J., Q. Zhou, N. Liu, Q. Gao, and Z. Guan, 2008: Teleconnection mode between IOD and Northern Hemisphere tropospheric circulation and its mechanism. *Meteor. Atmos. Phys.*, **100**, 207–215, https://doi.org/10.1007/s00703-008-0304-9.

Nishihira, G., and S. Sugimoto, 2022: Severe cold winters in East Asia linked to first winter of La Niña events and in North America linked to second winter. *Geophys. Res. Lett.*, **49**, e2021GL095334, https://doi.org/10.1029/2021GL095334.

Okumura, Y. M., and C. Deser, 2010: Asymmetry in the duration of El Niño and La Niña. *J. Climate*, **23**, 5826–5843, https://doi.org/10.1175/2010JCLI3592.1.

——, P. DiNezio, and C. Deser, 2017: Evolving impacts of multi-year La Niña events on atmospheric circulation and U.S. drought. *Geophys. Res. Lett.*, **44**, 11 614–11 623, https://doi.org/10.1002/2017GL075034.

Pinto, J. G., M. Reyers, and U. Ulbrich, 2011: The variable link between PNA and NAO in observations and in multi-century CGCM simulations. *Climate Dyn.*, **36**, 337–354, https://doi.org/10.1007/s00382-010-0770-x.

Rayner, N. A., D. E. Parker, E. B. Horton, C. K. Folland, L. V. Alexander, D. P. Rowell, E. C. Kent, and A. Kaplan, 2003: Global analyses of sea surface temperature, sea ice, and night marine air temperature since the late nineteenth century. *J. Geophys. Res.*, **108**, 4407, https://doi.org/10.1029/2002JD002670.

Ropelewski, C. F., and M. S. Halpert, 1986: North American precipitation and temperature patterns associated with the El Niño/Southern Oscillation (ENSO). *Mon. Wea. Rev.*, **114**, 2352–2362, https://doi.org/10.1175/1520-0493(1986)114<2352:NAPATP>2.0.CO;2.

Saji, N. H., B. N. Goswami, P. N. Vinayachandran, and T. Yamagata, 1999: A dipole mode in the tropical Indian Ocean. *Nature*, **401**, 360–363, https://doi.org/10.1038/43854.

Stachnik, J. P., and C. Schumacher, 2011: A comparison of the Hadley circulation in modern reanalyses. *J. Geophys. Res.*, **116**, D22102, https://doi.org/10.1029/2011JD016677.

Stephenson, D. B., V. Pavan, M. Collins, M. M. Junge, and R. Quadrelli, and Participating CMIP2 Modelling Groups, 2006: North Atlantic Oscillation response to transient greenhouse gas forcing and the impact on European winter climate: A CMIP2 multi-model assessment. *Climate Dyn.*, **27**, 401–420, https://doi.org/10.1007/s00382-006-0140-x.

Vimont, D. J., J. M. Wallace, and D. S. Battisti, 2003: The seasonal footprinting mechanism in the Pacific: Implications for ENSO. *J. Climate*, **16**, 2668–2675, https://doi.org/10.1175/1520-0442(2003)016<2668:TSFMIT>2.0.CO;2.

Wallace, J. M., and D. S. Gutzler, 1981: Teleconnections in the geopotential height field during the Northern Hemisphere winter. *Mon. Wea. Rev.*, **109**, 784–812, https://doi.org/10.1175/1520-0493(1981)109<0784:TITGHF>2.0.CO;2.

Yang, S., Z. Li, J.-Y. Yu, X. Hu, W. Dong, and S. He, 2018: El Niño–Southern Oscillation and its impact in the changing climate. *Natl. Sci. Rev.*, **5**, 840–857, https://doi.org/10.1093/nsr/nwy046.

Yu, J.-Y., and H.-Y. Kao, 2007: Decadal changes of ENSO persistence barrier in SST and ocean heat content indices: 1958–2001. *J. Geophys. Res.*, **112**, D13106, https://doi.org/10.1029/2006JD007654.

——, and S.-W. Fang, 2018: The distinct contributions of the seasonal footprinting and charged-discharged mechanisms to ENSO complexity. *Geophys. Res. Lett.*, **45**, 6611–6618, https://doi.org/10.1029/2018GL077664.

——, Y. Zou, S. T. Kim, and T. Lee, 2012: The changing impact of El Niño on US winter temperatures. *Geophys. Res. Lett.*, **39**, L15702, https://doi.org/10.1029/2012GL052483.

Yuan, X., 2004: ENSO-related impacts on Antarctic sea ice: A synthesis of phenomenon and mechanisms. *Antarct. Sci.*, **16**, 415–425, https://doi.org/10.1017/S0954102004002238.

Zhang, T., J. Perlwitz, and M. P. Hoerling, 2014: What is responsible for the strong observed asymmetry in teleconnections between El Niño and La Niña? *Geophys. Res. Lett.*, **41**, 1019–1025, https://doi.org/10.1002/2013GL058964.

Zhang, Y., W. Zhou, X. Wang, S. Chen, J. Chen, and S. Li, 2022a: Indian Ocean dipole and ENSO's mechanistic importance in modulating the ensuing-summer precipitation over eastern China. *npj Climate Atmos. Sci.*, **5**, 48, https://doi.org/10.1038/s41612-022-00271-5.

——, ——, ——, X. Wang, R. Zhang, Y. Li, and J. Gan, 2022b: IOD, ENSO, and seasonal precipitation variation over eastern China. *Atmos. Res.*, **270**, 106042, https://doi.org/10.1016/j.atmosres.2022.106042.

Zhao, Y., and D.-Z. Sun, 2022: ENSO asymmetry in CMIP6 models. *J. Climate*, **35**, 5555–5572, https://doi.org/10.1175/JCLI-D-21-0835.1.

Zhu, T., and J.-Y. Yu, 2022: A shifting tripolar pattern of Antarctic sea ice concentration anomalies during multi-year La Niña events. *Geophys. Res. Lett.*, **49**, e2022GL101217, https://doi.org/10.1029/2022GL101217.